Research Article | Vol. 29, No. 15 / 19 July 2021 / Optics Express 23622
Optics EXPRESS

Understanding bending-induced loss and bending-enhanced higher-order mode suppression in negative curvature fibers

YUXI WANG AND WONKEUN CHANG*

School of Electrical and Electronic Engineering, Nanyang Technological University, 639798, Singapore
**wonkeun.chang@ntu.edu.sg*

Abstract: We present a numerical analysis on bending-induced loss and bending-enhanced higher-order mode suppression in negative curvature fibers. We provide underlying mechanisms on how geometrical parameters affect the bending properties. We find that fiber parameters influence the bending performance by altering the resonant coupling conditions, as well as light leakage through inter-tube gaps. We identify regions in the parameter space that exhibit excellent bending properties and offer general guidelines for designing negative curvature fibers that are less sensitive to bending. Moreover, we explore the possibility of enhancing higher-order core mode suppression through mechanical bending. We find that up to nine-fold increase in the higher-order mode extinction ratio can be achieved by bending the fiber.

1. Introduction

Negative curvature hollow core fibers have attracted a great deal of interest in the past several years as an excellent light-guiding platform [1,2]. Their unique properties such as low loss, broadband guidance, and small nonlinearity make them promising for various applications, including in high power beam delivery [3–5], guided optics in vacuum-ultraviolet and mid-infrared [6–10], and telecommunications [11].

Many efforts have been made to optimize the light guiding properties of negative curvature fibers resulting in emergence of several different negative curvature fiber designs [12–18]. Wang et al. first observed a substantial reduction in the transmission loss in a kagome fiber by surrounding its core with dielectric strands in a hypocycloid shape [12]. Pryamikov et al. reported the first negative curvature fiber that consists only of tubular cladding elements surrounding the central hollow core [13]. These two base designs became the mainstream in the hollow core fiber research nowadays. The presence of negative curvatures at the core cladding interface and absence of Fano resonances by separating the tubular elements apart with a small gap between them are the key structural features that allow low transmission loss and broadband guidance [12,13,18–20]. Further improvement in terms of loss and modal properties have been achieved by inserting an additional tube in each cladding element to form a nested geometry [21–23], demonstrating extremely low loss of only 0.28 dB·km^{-1} in C and L bands [24].

Mechanical flexibility is one of the main merits of fiber optics. The bending introduces additional loss and may also alter the modal properties. Past investigations have shown that the bending properties of negative curvature fiber depend strongly on its cross-sectional geometry [21,25–32]. For instance, varying the core size, altering the size of the cladding elements, as well as introducing nested cladding elements all have considerable impact on the bending properties of the fiber. Therefore, a well-thought-out choice of the structural parameters can ensure optimum bending performance.

Belardi et al. first reported that negative curvature fiber with non-touching tubes can have relatively low bending loss [25]. The same work also found that varying the size of cladding tubes has significant effect on the bending sensitivity. Gao et al. also demonstrated a six-tube negative

#432314 https://doi.org/10.1364/OE.432314
Journal © 2021 Received 24 May 2021; revised 25 Jun 2021; accepted 28 Jun 2021; published 9 Jul 2021

Optics EXPRESS

curvature fiber with low bending loss under tight bending condition in the short wavelength side close to the edge of the transmission band [26]. Wei et al. presented a numerical study on the bending loss, varying the bending direction, thickness of the cladding tube wall, as well as polarization direction of the light [27]. It was also revealed that adding another layer of dielectric tubes in the cladding can substantially reduce the bending loss [28,29].

Under mechanical bending, the effective index changes along the axis of bending direction. This may give rise to bending-induced resonant couplings between the modes in the hollow core and those in the hollow regions in cladding elements, increasing the loss by several orders of magnitude. The first observation of such phenomenon in negative curvature hollow core fiber was reported in Kosolapov et al. [33]. Similar bending-induced resonant coupling was also discussed in a kagome-lattice hollow core fiber [34], and a subsequent systematic study on bending loss in this type of fiber followed soon after [35]. In tubular geometries, the resonant coupling behavior was first examined in a THz waveguide [30]. Later, Frosz et al. derived an analytical formula approximating the critical bending radius at which the resonant coupling occurs [31], and Carter et al. experimentally confirmed the bending-induced resonant coupling in tubular negative curvature fibers [32].

In this work, we present a systematic and comprehensive numerical study on how the structural parameters affect the light guiding properties of negative curvature fibers under mechanical bending. We investigate the effect of changing number and size of cladding tubes, bending orientation, core size, as well as having nested elements in the cladding. Modifying these geometrical parameters alters the resonant coupling condition, and we identify the regions where low bending-induced loss can be realized. Moreover, we evaluate the possibility of using mechanical bending to change the modal properties in negative curvature fiber and filter out higher-order core modes. Indeed, a couple of past studies have considered bending as a means to realize single-mode guidance [4,31]. Here, we give a detailed numerical encounter of the bending-enhanced higher-order mode suppression in negative curvature fibers.

2. Geometrical formulation and numerical method

We analyze two kinds of negative curvature fibers that are studied extensively. One is the tubular negative curvature fiber (TNCF) [18] and the other is the nested antiresonant nodeless fiber (NANF) [21]. Their idealized cross-sections are depicted in Fig. 1. They are characterized by the core diameter, D, which is the diameter of the largest circle that fits in the central hollow region, set to 40 μm in this work if not specified. t is dielectric wall thickness of the cladding elements, which we use 0.4 μm. The number of cladding elements surrounding the core, N, is limited to three commonly used cases, i.e., $N = 6$, 7, and 8. d is defined as the exterior diameter of the cladding elements in TNCF, and that of the outer cladding elements in NANF. d' in NANF is the diameter of the inner cladding elements, and we set $d = 2d'$ following the past fabrication practices [24]. The wavelength is λ, and we use 1.68 μm throughout this work unless mentioned otherwise. This value is chosen to ensure that the guidance is in the middle of the first transmission band in the antiresonant hollow core fibers for the dielectric cladding wall thickness used in our work [20], which is given by $\lambda = 4t(n^2 - 1)^{0.5}$ where n is the index of the waveguide material. We set the material to be silica throughout this work.

We assume the bending occurs in the positive x direction as illustrated in Fig. 1. The bending is characterized by the bending radius, R and angular orientation of the fiber with respect to the bending direction, θ. Latter is the angle between the x-axis and center of the cladding element that is nearest the x-axis. The range of possible bending orientation is then $0 \leq \theta \leq \pi/N$ [31]. While the loss under mechanical-bending in the x- and y-polarized fundamental core modes are not the same, the difference is relatively small and have the same qualitative features as we shall show in the next section. Therefore, we consider only the y-polarized mode in this study.

Optics EXPRESS

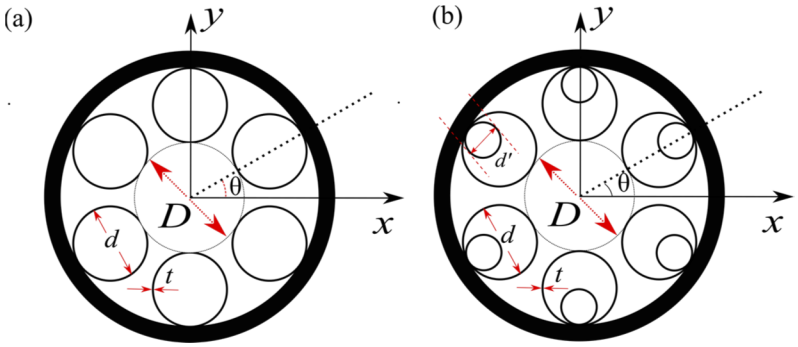

Fig. 1. Idealized cross-sections of (a) TNCF and (b) NANF when the number of cladding elements, $N = 6$. t is the wall thickness of the dielectric cladding tubes, d is the exterior diameter of the cladding tubes in TNCF. In NANF, d and d' are the exterior diameters of the outer and inner cladding tubes, respectively. Bending is assumed in the positive x direction, where θ denotes the bending orientation. It is the angle between x-axis and center of the cladding element that is nearest the x-axis.

The conformal mapping technique is applied to calculate the loss induced in the fundamental and higher-order modes under mechanical bending [36–38]. The equivalent refractive index, $n'(x, y)$, under bending at position x from the fiber center is calculated by:

$$n'(x, y) = n(x, y)\left(1 + \frac{x}{R}\right), \tag{1}$$

where $n(x, y)$ is the refractive index at position (x, y) in the cross section of the straight fiber. For the numerical investigation, we use the finite-element modeling to compute the bending-induced loss in the fundamental and higher-order modes. This is obtained by first calculating the confinement loss of the fiber when it is straight and subtract it from the loss calculated under bending. By doing so, we can extract only the impact of mechanical bending on the guidance. To ensure the numerical accuracy and stability, the maximum mesh size is kept below $\lambda/6$ in the dielectric material and $\lambda/4$ in the hollow regions. Additionally, we carry out extensive convergence tests to ensure numerical reliability.

3. Bending-induced loss

3.1. Number and size of dielectric cladding tubes

Shown in Figs. 2(a)–2(c) are the false colormaps of the bending-induced loss in TNCF with d/D in the vertical axis and R in the horizontal axis for $N = 6$, 7, and 8, respectively. Note the maximum achievable d/D is given by $\sin(\pi/N)/(1 - \sin(\pi/N))$, and it decreases as N is increased [39]. Hence the range of possible d/D is the largest out of the three cases considered when $N = 6$ and smallest when $N = 8$. We set $\theta = \pi/N$ for now. A discussion on the effect of bending orientation is presented in the next subsection.

One of the most prominent features in Figs. 2(a)–2(c) is the presence of a narrow band of very high bending-induced loss. This is labelled II in Fig. 2(a), and its location remains almost identical in Figs. 2(b) and 2(c) albeit its upper extent is cut short by the smaller maximum achievable d/D at larger N values. They correspond to bending-induced mode coupling between the fundamental core mode and cladding hole mode (HE_{11}), leading to considerable light leakage from the core [30]. The intensity profile of the fundamental mode in this instance is shown in the inset labeled II in Fig. 2(a). At this specific bending orientation, the hole modes from the two neighboring cladding tubes couple simultaneously as we shall discussed in detail in the

Optics EXPRESS

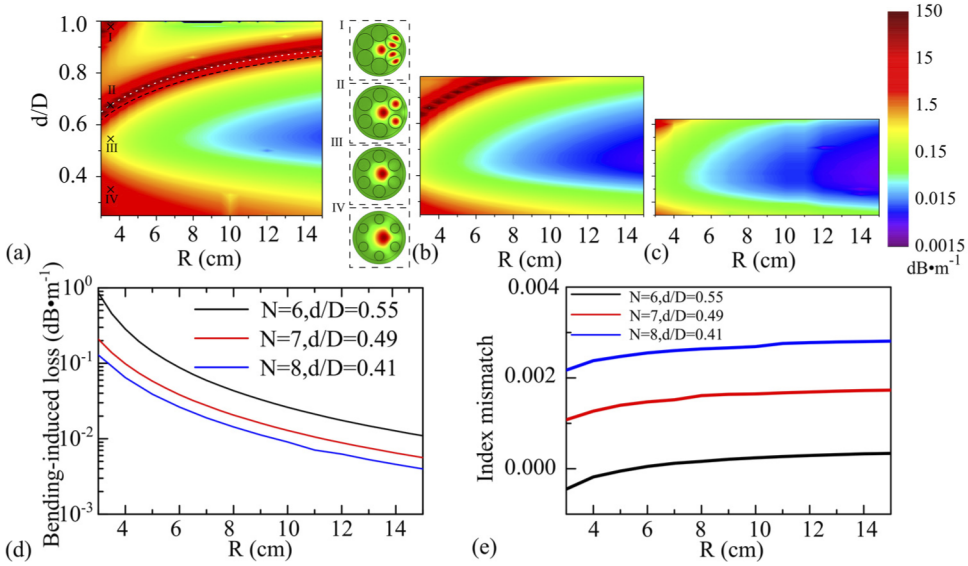

Fig. 2. False colormaps of bending-induced loss in the fundamental core mode of TNCF against d/D and R for (a) $N = 6$, (b) $N = 7$, and (c) $N = 8$. The other geometrical parameters are set at $D = 40$ μm, $t = 0.4$ μm, $\theta = \pi/N$, and $\lambda = 1.68$ μm. The insets in (a) show the intensity profiles of the fundamental mode for different d/D values at a tight bending condition, illustrating different regimes. (d) Bending-induced loss in the fundamental core mode and (e) index mismatch between the fundamental core mode and HE_{11} cladding hole mode of TNCF as a function of R for $N = 6$, 7, and 8. In each N, d/D is set to a value that exhibits the best bending performance, i.e., 0.55, 0.49, 0.41, respectively.

next subsection. The resonant coupling happens when index mismatch between the two modes becomes zero as the bending distorts the refractive index profile of the fiber along the x-direction. Ref. [31] discusses a detailed encounter of this phenomenon, and presents an analytically derived formula for estimating the critical bending radius, R_{cr}, which is given by:

$$R_{cr} = \frac{D^3\pi^2(d_{in}/D)^2}{\lambda^2 u_{01}^2(1-d_{in}/D)}\cos\theta \text{ or } \frac{R_{cr}}{\lambda} = \frac{\pi^2(d_{in}/D)^2}{u_{01}^2(1-d_{in}/D)}\cos\theta\left(\frac{D}{\lambda}\right)^3, \quad (2)$$

where u_{01} is the first zero of the Bessel function, J_0. $d_{in} = d - 2t$, and it is the interior diameter of the cladding elements. Eq. (2) implies that R_{cr}/λ scales with $(D/\lambda)^3$. The locations of R_{cr} in the case of $N = 6$ is indicated by a black-dashed line in Fig. 2(a). We note that there is a small mismatch between the analytically predicted R_{cr} and the numerically observed bending-induced resonant coupling loss peak. This can be adjusted by multiplying a correction factor of 0.84 to Eq. (2), improving the agreement as shown with a white-dotted line in Fig. 2(a). Here, we observe that as d/D is reduced R_{cr} decreases, i.e., the fiber becomes less sensitive to bending. The index difference between the fundamental core mode and cladding hole mode of the straight fiber increases as the discrepancy in the physical size between the two hollow regions becomes larger. This leads to requiring more bending-induced index distortion to achieve the resonant coupling. Below a certain d/D, no resonant couplings can occur even at tight bending conditions of R<3 cm.

For the same reason, there is a relatively large region of low bending-induced loss, labeled III, below R_{cr} in each N, where the interaction between the fundamental core and cladding hole modes is weak. An example intensity profile of the well-isolated fundamental mode in this region is shown in the inset labeled III in Fig. 2(a). This happens at around $d/D = 0.55$, 0.49, and 0.41

Optics EXPRESS

when $N = 6$, 7, and 8, respectively, exhibiting the best bending loss property in each N. These are the cladding to core size ratios that should be considered when robust transmission against mechanical bending is of high importance in TNCF. The bending-induced loss versus R plots are presented in Fig. 2(d) for these three d/D values. We observe that the fiber becomes less sensitive to bending as N is increased. The index mismatch between the fundamental core mode and cladding hole modes of unbent fiber becomes larger against N as shown in Fig. 2(e). The bigger mismatch requires more severe bending-induced distortion to induce coupling, making it more robust against bending.

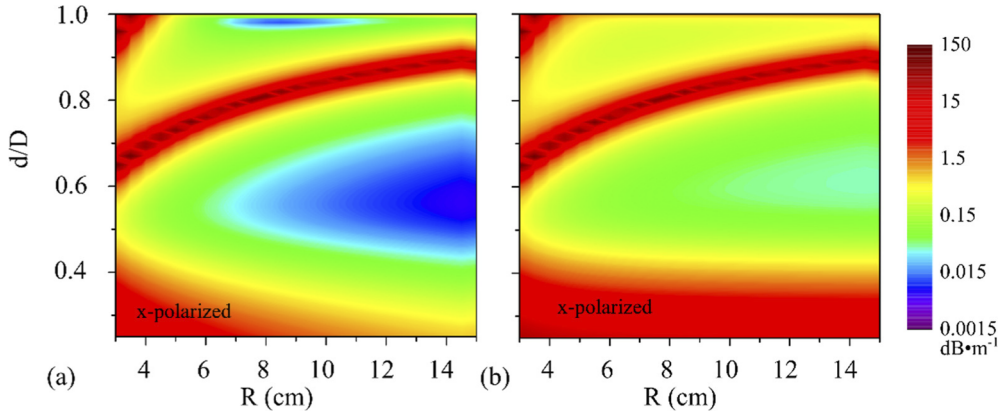

Fig. 3. (a) False colormap of bending-induced loss in the fundamental core mode of TNCF with varying d/D and R. The parameters are identical to those used in Fig. 2(a), i.e., $N = 6$, $D = 40$ μm, $t = 0.4$ μm, $\theta = \pi/N$, and $\lambda = 1.68$ μm, albeit x-polarized fundamental core mode is presented instead of the y-polarized mode. (b) Loss of the bent fiber with the same set of parameters used in (a). This is the loss obtained from the finite-element modeling on the bent fiber before subtracting it from the loss in the straight fiber.

Moving further down d/D, there is another regime where the bending-induced loss starts to rise again. In other words, TNCF becomes increasingly sensitive to bending when the size of the cladding elements gets too small. The gap between the cladding elements becomes bigger, and the light leakage through the gaps starts to dominate the bending-induced loss. This is clearly identified in the inset labeled IV in Fig. 2(a), which captures the light in the fundamental core mode leaking through the gaps.

In the top left corner in Fig. 2(a), labeled I, where the bending is tight (R<4 cm) and the cladding tubes are large (d/D>0.9), there exists another high loss band that is related to the bending-induced resonant coupling between the fundamental core mode and a higher-order cladding hole mode. The intensity profile of the fundamental core mode of this interaction is presented in the inset labeled I in Fig. 2(a). Note that the resonant coupling to the higher-order cladding modes occurs only in $N = 6$ in Fig. 2, as the cladding tubes in N>6 are too small to support this type of coupling. In the subsequent subsections, we will see more examples of resonant couplings between fundamental core and various higher-order cladding modes. These findings are consistent with analytical and experimental results reported in Ref. [32].

At this point, we check the differences in the bending loss properties between the two orthogonally polarized fundamental core modes. Figure 3(a) is a false colormap of the bending-induced loss for x-polarized fundamental core mode. All other parameters are same as in Fig. 2(a), and hence a direct comparison between Figs. 2(a) and 3(a) can be made. It is apparent from the two plots that there are very little differences between the two orthogonally polarized modes. Figure 3(b) is a false colormap of the loss of the bent fiber with the same set of parameters used in Fig. 3(a). This is the loss obtained directly from the finite-element modeling of the bent fiber

Optics EXPRESS

before subtracting it from the loss in the straight fiber. There is a general increase in the loss in Fig. 3(b) since the loss in the straight fiber is added onto the bending-induced loss. However, the qualitative features remain mostly the same.

3.2. Bending orientation

Past studies on the bending-induced loss have been discussed mainly under two extreme bending orientations, i.e., $\theta = 0$ and π/N [26,31]. However, in practice, θ can be of any arbitrary angle between 0 and π/N. In addition to these two extremes, here we also study two intermediate orientations to gain more general understanding. The results are presented as false colormaps in Fig. 4 against varying d/D and R for TNCF with $N = 6$. Namely, Figs. 4(a)–4(d) shows, respectively, the bending-induced loss for $\theta = \pi/N$ and 0, i.e., the two extremes, and the two intermediate orientations of $\theta = \pi/(3N)$ and $2\pi/(3N)$.

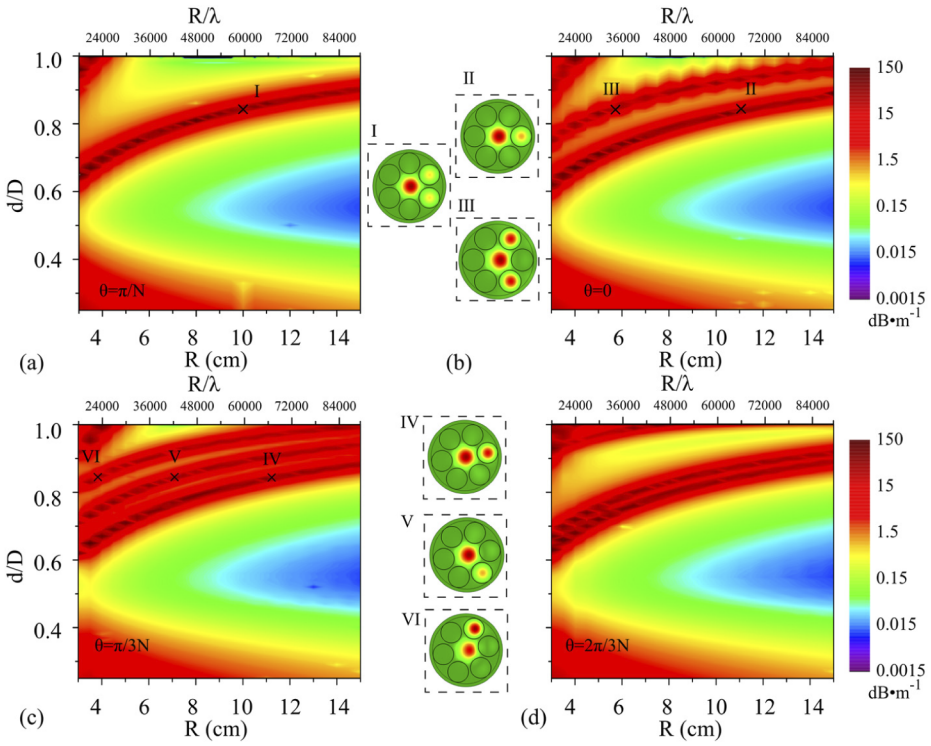

Fig. 4. False colormaps of bending-induced loss in the fundamental core mode of TNCF with varying d/D and R. The bending orientations are (a) $\theta = \pi/N$, (b) $\theta = 0$, (c) $\theta = \pi/(3N)$, and (d) $\theta = 2\pi/(3N)$. The other parameters are set at $N = 6$, $D = 40$ μm, $t = 0.4$ μm, and $\lambda = 1.68$ μm. The insets show the intensity profiles of the fundamental core mode at different resonant couplings.

As R is reduced, the fundamental core mode sequentially interacts with the hole modes of the cladding elements that are in the same quadrant as the bending direction, $+x$. The sequence of coupling depends on the angle between the cladding tube involved and x-axis. The basic rule is that the coupling occurs first with the cladding element that is the nearest to the bending direction. Then as R is reduced the elements that are further away successively interact with the fundamental core mode.

In the case $\theta = \pi/N$, the cladding elements are arranged symmetrically around the bending direction. Hence, the high bending-induced loss region labeled I in Fig. 4(a) arises due to the

Optics EXPRESS

fundamental core mode coupling simultaneously to two cladding element modes that are equally separated apart from the x-axis. The intensity profile of this resonant coupling is shown in the inset labeled I in Fig. 4(a). This degeneracy leads to a narrower range of the high bending-induced region compared to other orientations. When $\theta = 0$, one of the cladding tubes is centered around the $+x$-axis, and hence resonant coupling to this tube first appears as R is decreased. This corresponds to the high loss region labeled II in Fig. 4(b). Further reduction in R leads to concurrent resonant couplings to the two adjacent cladding tubes. Again, this degeneracy shows up as a single loss peak labeled III in Fig. 4(b).

For general bending orientations, the symmetry around the $+x$-axis does not exist. Hence in most cases, the bending-induced resonant coupling to cladding tubes occurs individually, each leading to a distinct loss peak. This is exemplified in Fig. 4(c) for $\theta = \pi/(3N)$ with three high loss bands labeled IV, V, and VI across a wide region. Coming down in R from a large value, the fundamental mode resonantly couples, first to the tube that is closest to the $+x$-axis, and successively to the neighboring cladding tubes in the order of their proximity to the bending direction as shown in the insets in Fig. 4(c). A similar observation is made in the case of $\theta = 2\pi/(3N)$ in Fig. 4(d).

Apart from the regions where the resonant couplings occur, the orientation has no major impact on the bending performance of TNCF.

3.3. Wavelength

Next, we study the effect of changing the wavelengths on the bending-induced loss. The false colormaps of the bending-induced loss for $\lambda = 1.06$ and 2.4 μm while other parameters are set at their usual values are shown in Figs. 5(a) and 5(b). Additionally, we can include Fig. 2(a) for $\lambda = 1.68$ μm in the comparison as the intermediate wavelength between the two. We note that $\lambda = 1.06$ and 2.4 μm are in the short- and long-wavelength sides of the first transmission band, respectively, in TNCF with $t = 0.4$ μm. The high-loss band labeled I in Fig. 5(a) is caused by the bending-induced resonant coupling to the HE_{11} mode in the cladding as shown in the inset. Similarly, the loss band labeled I in Fig. 5(b) is due to the same bending-induced mode coupling. Other high loss bands due to the resonant couplings to the higher-order hole modes in the cladding elements are illustrated and labeled correspondingly in the insets in Fig. 5(a). Note that the couplings to the higher-order hole modes in the cladding tubes do not appear for $\lambda = 2.4$ μm within the range of parameters studied. The black region in the top left corner in Fig. 5(b) is where the bending-induced loss is negative, i.e., bending reduces the loss. This happens because, when d/D is close to 1, the index of the cladding hole mode is almost identical to that of the fundamental core mode in the unbent fiber. Hence, the bending-induced distortion increases the index difference between the two, which improves the light confinement in the core. Other general features are similar at different wavelengths, except that TNCF becomes more sensitive to bending at shorter wavelengths, i.e., R_{cr} shifts to larger R, which is in-line with Eq. (2). The bending-induced loss at 2.4 μm is lower than at $\lambda = 1.06$ μm. The ideal cladding to core size ratio of $d/D = 0.55$ remains almost the same between the two wavelengths.

Figures 5(c) and 5(d) show the bending-induced loss at two R values of 3 and 10 cm over a wide spectral range from 1 to 2.7 μm. In both cases, the range of d/D below the high loss region labeled I where TNCF is resistant to mechanical bending becomes smaller as the wavelength is decreased. For example, when $d/D = 0.64$, TNCF is resistant to bending even at tight bending condition, i.e., 3 cm, at $\lambda = 2.4$ μm, but the same fiber resonant couples to HE_{11} cladding mode at $\lambda = 1.68$ μm as indicated with A and A' in Fig. 5(c). We also note that resonant couplings to higher-order cladding hole modes can be eliminated at longer wavelengths. Nevertheless, even under a tight bending condition, TNCF can be designed to operate with relatively low bending-induced loss as shown in Fig. 5(c).

Optics EXPRESS

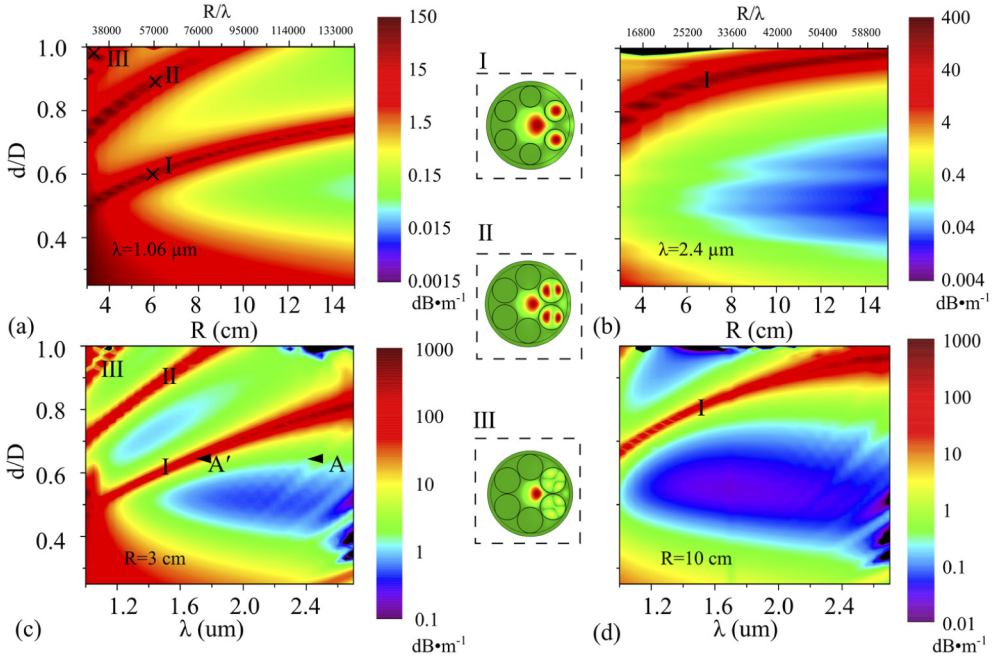

Fig. 5. False colormaps of bending-induced loss in the fundamental mode of TNCF for varying d/D and R. The wavelengths are (a) $\lambda = 1.06$ μm and (b) $\lambda = 2.4$ μm. The other parameters are $N = 6$, $D = 40$ μm, $t = 0.4$ μm, and $\theta = \pi/N$. The false colormaps for varying d/D and λ, keeping the remaining parameters the same are shown for (c) $R = 3$ cm and (d) $R = 10$ cm.

We point out when the wavelength is changed, it also changes the core size relative to the wavelength. This means the effect of changing wavelength is similar to changing the core size. This is discussed in the next subsection.

3.4. Core size

It is well understood that the confinement loss in an unbent TNCF has a strong dependence on the core size, with the larger core exhibiting smaller loss in general [2,40,41]. Let us look at then how the core size affects the bending-induced loss. Figures 6(a)–6(c) present the false colormaps of the bending-induced loss in TNCF with $N = 6$ for d/D versus R at three different core sizes, i.e., $D = 30$, 50, and 60 μm. We set $\theta = \pi/N$ and hence we can also include the plot for $D = 40$ μm shown in Fig. 2(a) in this comparison. The core diameter to wavelength ratios, D/λ, then ranges from 17.9 to 35.7. Since R_{cr}/λ scales with $(D/\lambda)^3$ in Eq. (2), our findings on the bending-induced resonant couplings can be applied directly to other wavelengths through the geometrical scaling of D/λ.

The comparison indicates clearly that enlarging the core alters the bending performance causing the resonant coupling condition to shift to a larger bending radius. For instance, when $d/D = 0.7$, R_{cr} values are around 4, 7, and 13 cm for $D = 40$, 50, and 60 μm, respectively. At $D = 30$ μm, R_{cr} drops below 3 cm. At the same time, the larger the core, the poorer the bending performance becomes. When $D = 30$ μm, the resonant coupling occurs only at large d/D, allowing for excellent light guidance down to very small R. In larger cores, on the other hand, the bending-induced resonant couplings appear in the range $0.5<d/D<0.7$ where most low-loss TNCFs are fabricated in practice, coming out to be the main limiting factor. The range of d/D that permits low bending-induced loss narrows as D is increased.

Optics EXPRESS

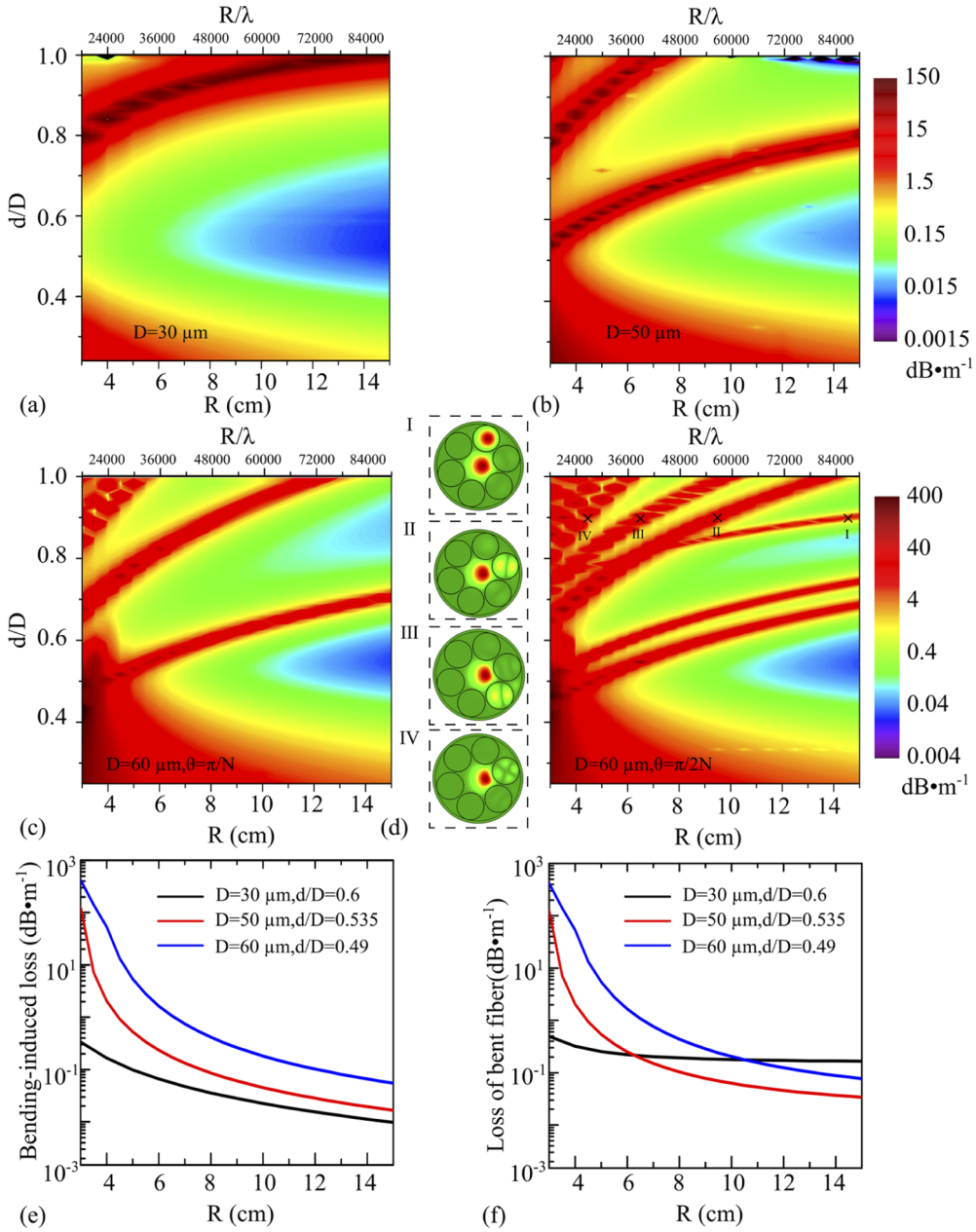

Fig. 6. False colormaps of bending-induced loss in the fundamental mode of TNCF with varying d/D and R. The core diameters are (a) $D = 30$ μm, (b) $D = 50$ μm, and (c) $D = 60$ μm. The other parameters are set at $N = 6$, $t = 0.4$ μm, $\theta = \pi/N$, and $\lambda = 1.68$ μm. We can include the plot for $D = 40$ μm in Fig. 2(a) in this comparison. (d) The same false colormap for $D = 60$ μm, $\theta = \pi/2N$ is presented to illustrate a more general bending orientation. The insets show the intensity profiles of the fundamental core mode at various bending-induced resonant couplings. (e) Bending-induced loss versus R at d/D that exhibits the smallest bending sensitivity for each D studied. (f) Loss of the bent fiber for the same set of parameters as in (e). This is the loss obtained from the finite element modeling on the bent fiber before subtracting it from the loss in the straight fiber.

Optics EXPRESS

One major difference observed in the false colormaps between different core sizes is the presence of bending-induced resonant couplings to higher-order cladding hole modes in larger core TNCFs. For a given d/D, the cladding tubes are also enlarged by the same amount in TNCFs when D is increased. This gives rise to higher-order cladding hole modes that can more easily couple to the fundamental core mode under bending.

We also investigate a case for an intermediate bending orientation of $\theta = \pi/(2N)$ at a larger core size as shown in Fig. 6(d). A mix of various bending-induced resonant couplings to a sequence of cladding tubes, as well as to higher-order cladding hole modes—illustrated in the insets—occur within the d/D and R ranges studied.

We pick an optimum d/D that exhibits the smallest bending sensitivity for each D studied and compare the bending-induced loss, as well as the loss in the bent fiber as a function of R. These are plotted in Figs. 6(e) and 6(f), respectively. We can clearly observe that TNCF with larger core shows higher bending-induced loss, while the loss contribution from the straight fiber is smaller. On the contrary, in a smaller core TNCF, the confinement loss in the straight fiber is the dominant cause contributing to the total loss, while the bending-induced loss can stay relatively low even at tight bending conditions.

3.5. Bending-induced loss in NANF

With remarkable recent advances in the fabrication of NANF, its transmission loss is now challenging that of conventional single-mode optical fibers [24]. It is expected to become a serious contender for use in fiber-optic communications. In this section, we present our numerical study on bending-induced resonant couplings in NANF.

Figure 7(a) shows the false colormap of the bending-induced loss in NANF with $N = 6$ for d/D versus R. The other parameters are set at $D = 30$ μm, $t = 0.4$ μm, $\theta = \pi\ /N$, and $\lambda = 1.55$ μm. The diameter of the nested element follows the diameter of the outer cladding tube such that $d' = d/2$. From Fig. 7(a), we can immediately see that the bending performance of NANF is much better than TNCF. The most noticeable difference is that the resonant couplings between the fundamental core mode and cladding hole modes happen only at very tight bending condition of R<2 cm across a wide range of d/D. This is because the hollow region inside the cladding elements is substantially altered by the presence of the nested tube, and the hole modes that appear have vastly different effective indices to that of the fundamental core mode. This makes them difficult to resonant couple to the fundamental core mode even under excessive bending-induced distortion. The region of low bending-induced loss is therefore very large in NANF. It exhibits the best bending performance when $d/D \approx 0.7$ where very low bending-induced loss can be achieved down to $R = 1$ cm. Nevertheless, the bending-induced resonant coupling still occurs at $R \approx 1$ cm for large d/D. An example of the interaction is shown in the inset in Fig. 7(a). The intensity profile of the fundamental mode indicates that the hole mode at play is not an ideal HE_{11} mode as in TNCF, but a mode of complex form which resides inside the main cladding tube but outside the nested element.

Resonant couplings hardly occur when $\lambda = 1.55$ μm as shown in Fig. 7(a). However, they can appear at shorter wavelengths. Fig. 7(b) shows the false colormap of the bending-induced loss over a wide bandwidth when $R = 3$ cm. The high bending-induced loss at $d/D = 0.907$ and $\lambda = 1.05$ μm, marked with a cross, is a result of the resonant coupling as illustrated in the inset. Through a careful selection of the d/D value, for instance 0.7 in the case shown in Fig. 7(b), we can maximize the spectral bandwidth that is free from the bending-induced resonant couplings. Nevertheless, NANF offers bending-insensitive guidance over a broad spectral window within a large range of d/D, i.e., from 0.6 to 0.9.

Optics EXPRESS

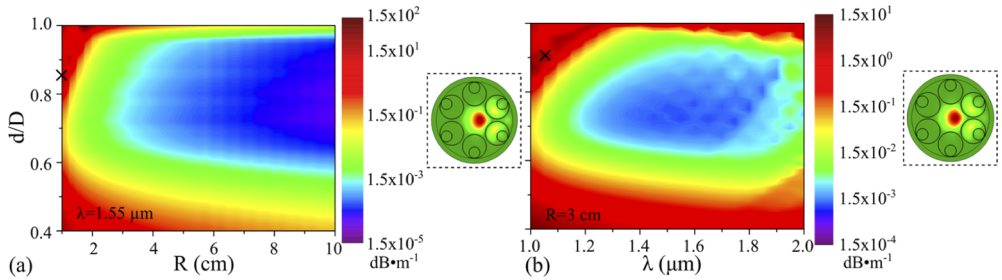

Fig. 7. False colormaps of bending-induced loss in the fundamental mode of NANF for varying d/D and (a) R when $\lambda = 1.55$ μm, and (b) λ when $R = 3$ cm. The other parameters are $N = 6$, $D = 30$ μm, $t = 0.4$ μm, $d' = d/2$, and $\theta = \pi/N$. The intensity profiles illustrating the fundamental core mode resonant couplings to a cladding hole mode at the positions marked with the crosses are shown in the insets.

4. Bending-induced higher-order mode suppression in TNCF

Loss in any specific modes can be varied by introducing mechanical bending of different amounts. We can exploit this property to effectively suppress unwanted modes, e.g., higher-order core modes. In a straight TNCF, Uebel et al. reports that higher-order modes can be strongly suppressed when $d/D = 0.68$ [42]. We investigate how we can yield effective single mode operation in TNCF through bending. We use the higher-order mode extinction ratio (HOMER), which is defined as the ratio of the lowest loss in higher-order modes to that in the fundamental mode, to quantify the effectiveness of higher-order mode suppression. Figures 8(a) and 8(b) are the plots showing HOMER versus $1/R$ in TNCF with $N = 6$ and 7, respectively. Three different values of d/D, i.e., 0.5, 0.6, and 0.7, are presented in each plot. The corresponding R is shown in the top axis where $1/R = 0$ is the unbent fiber. Hence, using this as a reference point, we can understand how bending influences HOMER. The other parameters are set at $D = 40$ μm, $t = 0.4$ μm, $\theta = \pi/N$, and $\lambda = 1.68$ μm. Figure 8 suggests that at moderate values of R>10 cm, the higher-order core modes can be more effectively suppressed than in unbent TNCFs in almost all cases. The bending-induced higher-order mode filtering works the best when $d/D = 0.6$. At smaller R, HOMER quickly drops below that of the unbent fiber, implying that there is a specific range of R in each TNCF geometry that can effectively eliminate the higher-order modes. The only exception out of those presented in Fig. 8 to this general trend is when $N = 7$ and $d/D = 0.7$ which exhibits poorer single-modedness when bent. This is because it happens to fall in the resonant coupling band as shown in Fig. 2(b) where the loss in the fundamental core mode is very high.

From Fig. 8, we can introduce a new indicator for the effectiveness of the higher-order mode suppression through bending. The bending-induced higher-order mode suppression ratio (BI-HOMER) is calculated by subtracting HOMER of the straight fiber from that of bent fiber. It is a quantity that measures by how much higher-order mode suppression improves through mechanical bending, such that a positive BI-HOMER means enhanced suppression through bending, and vice versa. With this, we study the effect of the core size on the bending-induced higher-order mode suppression. Figures 9(a) and 9(b) are false colormaps showing BI-HOMER in TNCF with $N = 6$ for d/D versus R at two different values of D, i.e., 30 and 50 μm. The plots suggest that bending can reinforce the higher-order mode suppression considerably over large area in the d/D-R plane. Namely, the red-shades denote the regions with BI-HOMER >10. When $D = 30$ μm, d/D that gives the best BI-HOMER is at around 0.6 over the entire range of R studied here, whereas when $D = 50$ μm, the optimum d/D varies with R, shifting slightly to a smaller value as R is reduced. This is because the optimum region for bending-induced

Optics EXPRESS

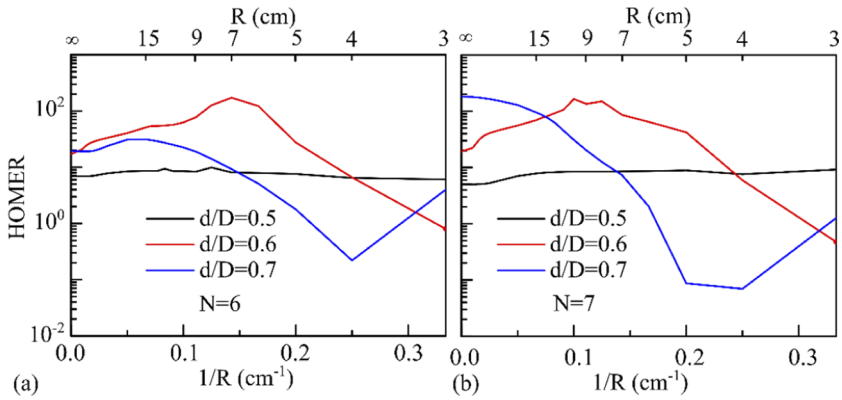

Fig. 8. HOMER versus $1/R$ in TNCF for different values of d/D when (a) $N = 6$ and (b) $N = 7$. The corresponding R is shown in the top axis. The other parameters are set at $D = 40$ μm, $t = 0.4$ μm, $\theta = \pi/N$, and $\lambda = 1.68$ μm.

higher-order mode suppression in $D = 50$ μm happens to coincide with the resonant coupling band as shown in Fig. 6(b), which diminishes the area where BI-HOMER is high. At large d/D, the higher-order mode suppression deteriorates with bending, i.e., BI-HOMER <0 (blue shades). This is where bending-induced resonant couplings to various cladding tubes and higher-order cladding hole modes occur. We note that HOMER-enhanced region (green and red shades) is much broader in Fig. 9(a), implying that the modal property under mechanical bending is better when the core is smaller.

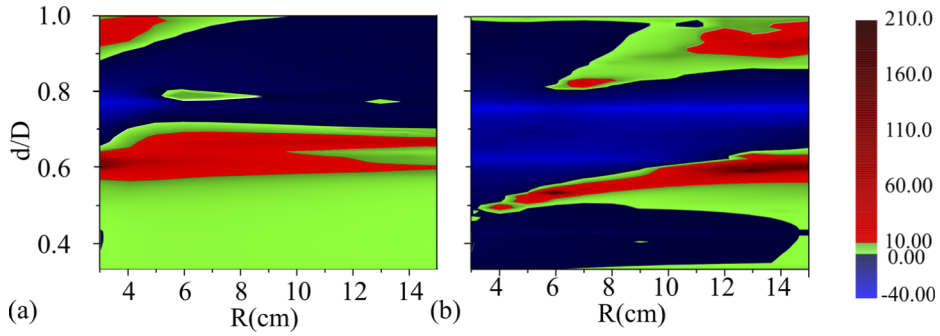

Fig. 9. False colormaps of BI-HOMER in TNCF for varying d/D and R. The core diameters are (a) $D = 30$ μm and (b) $D = 50$ μm. The other parameters are $N = 6$, $t = 0.4$ μm, $\theta = \pi/N$, and $\lambda = 1.68$ μm. The regions with BI-HOMER >10 are shaded in red, indicating strong enhancement in the higher-order mode suppression due to bending. The blue shades correspond to BI-HOMER <0, where the bending reduces HOMER. Green shaded regions mark moderate improvement in HOMER, i.e., 0< BI-HOMER <10.

Figures 10 shows how enhancement of the higher-order mode suppression through bending fairs with different number of cladding elements. The false colormaps of BI-HOMER for varying d/D and R are presented when $N = 6$, 7, and 8 in Figs. 10(a)–10(c), respectively. The highest BI-HOMER occurs at around $d/D = 0.6$ and $R = 7$ cm for all N, and we can achieve up to nine-fold increase in HOMER compared to the unbent case. The BI-HOMER enhanced areas are remarkably similar between the three plots, which indicates that the size of d is the most influential parameter on the modal property of TNCF under mechanical bending.

Optics EXPRESS

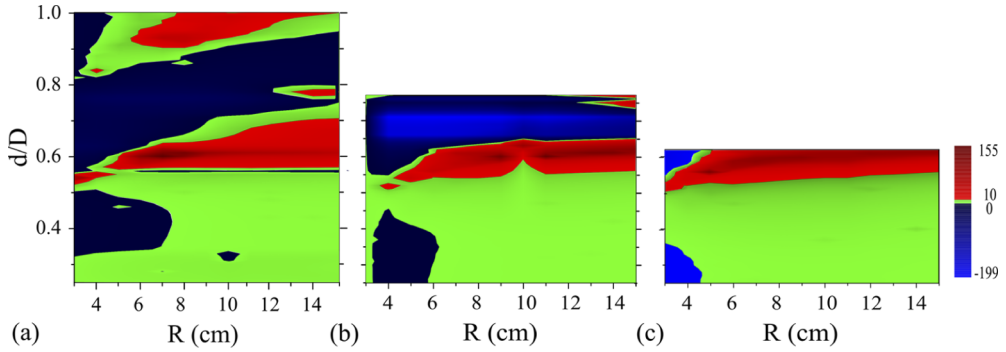

Fig. 10. False colormaps of BI-HOMER in TNCF for varying d/D and R. The number of cladding elements are (a) $N = 6$, (b) $N = 7$, and (c) $N = 8$. The other parameters are $D = 40$ µm, $t = 0.4$ µm, $\theta = \pi/N$, and $\lambda = 1.68$ µm. The areas with BI-HOMER >10 are shaded in red denoting strong enhancement in the higher-order mode suppression through bending. The blue shades correspond to BI-HOMER <0, where the bending reduces HOMER. Green shaded regions mark moderate improvement in HOMER, i.e., 0< BI-HOMER <10.

5. Conclusions

We present a detailed analysis of bending-induced loss and bending-enhanced higher-order mode suppression in negative curvature fibers. It provides a comprehensive picture of the relationships between various geometrical parameters and guiding properties of negative curvature fibers under mechanical bending. Overall, it is the effect of interactions between fundamental core mode and cladding hole modes—caused by the bending-induced index deformation—that ultimately determines the bending performance of negative curvature fibers. We identify regions in the parameter space where negative curvature fibers exhibit low bending-induced loss even under tight bending conditions. The findings can be used as a general guideline for designing negative curvature fibers where bending insensitive guidance is of high importance. Furthermore, we explore the possibility of using mechanical bending to enhance the suppression of higher-order core modes in negative curvature fibers. We can achieve up to nine-fold increase in the higher-order mode extinction ratio by bending the fiber to induce resonant coupling between the higher-order core modes and cladding hole modes.

Funding. National Research Foundation Singapore (QEP-P4).

Disclosures. The authors declare no conflicts of interest.

Data availability. Data underlying the results presented in this paper are not publicly available at this time but may be obtained from the authors upon reasonable request.

References

1. C. Wei, R. J. Weiblen, C. R. Menyuk, and J. Hu, "Negative curvature fibers," Adv. Opt. Photonics **9**(3), 504–561 (2017)..
2. F. Yu and J. C. Knight, "Negative Curvature Hollow-Core Optical Fiber," IEEE J. Sel. Top. Quantum Electron. **22**(2), 146–155 (2016).
3. B. Debord, M. Alharbi, L. Vincetti, A. Husakou, C. Fourcade-Dutin, C. Hoenninger, E. Mottay, F. Gérôme, and F. Benabid, "Multi-meter fiber-delivery and pulse self-compression of milli-joule femtosecond laser and fiber-aided laser machining," Opt. Express **22**(9), 10735–10746 (2014)..
4. M. Michieletto, J. K. Lyngsø, C. Jakobsen, J. Lægsgaard, O. Bang, and T. T. Alkeskjold, "Hollow-core fibers for high power pulse delivery," Opt. Express **24**(7), 7103–7119 (2016)..
5. X. Zhu, D. Wu, Y. Wang, F. Yu, Q. Li, Y. Qi, J. Knight, S. Chen, and L. Hu, "Delivery of CW laser power up to 300 watts at 1080 nm by an uncooled low-loss anti-resonant hollow-core fiber," Opt. Express **29**(2), 1492–1501 (2021)..
6. D. Xiong, J. Luo, M. R. A. Hassan, X. Wu, and W. Chang, "Low-energy-threshold deep-ultraviolet generation in a small-mode-area hollow-core fiber," Photonics Res. **9**(4), 590–595 (2021)..

Optics EXPRESS

7. T. Gavara, M. I. Hasan, M. R. A. Hassan, A. Deng, and W. Chang, "Band-edge mediated frequency down-conversion in a gas-filled anti-resonant hollow-core fiber," Opt. Lett. **45**(24), 6815–6818 (2020)..
8. P. S. J. Russell, P. Hölzer, W. Chang, A. Abdolvand, and J. C. Travers, "Hollow-core photonic crystal fibres for gas-based nonlinear optics," Nat. Photonics **8**(4), 278–286 (2014)..
9. M. R. A. Hassan, F. Yu, W. J. Wadsworth, and J. C. Knight, "Cavity-based mid-IR fiber gas laser pumped by a diode laser," Optica **3**(3), 218–221 (2016)..
10. A. I. Adamu, M. S. Habib, C. R. Petersen, J. E. A. Lopez, B. Zhou, A. Schülzgen, M. Bache, R. Amezcua-Correa, O. Bang, and C. Markos, "Deep-UV to mid-IR supercontinuum generation driven by mid-IR ultrashort pulses in a gas-filled hollow-core fiber," Sci. Rep. **9**(1), 4446 (2019)..
11. F. Poletti, N. V. Wheeler, M. N. Petrovich, N. Baddela, E. Numkam Fokoua, J. R. Hayes, D. R. Gray, Z. Li, R. Slavík, and D. J. Richardson, "Towards high-capacity fibre-optic communications at the speed of light in vacuum," Nat. Photonics **7**(4), 279–284 (2013)..
12. Y. Y. Wang, N. V. Wheeler, F. Couny, P. J. Roberts, and F. Benabid, "Low loss broadband transmission in hypocycloid-core Kagome hollow-core photonic crystal fiber," Opt. Lett. **36**(5), 669–671 (2011)..
13. A. D. Pryamikov, A. S. Biriukov, A. F. Kosolapov, V. G. Plotnichenko, S. L. Semjonov, and E. M. Dianov, "Demonstration of a waveguide regime for a silica hollow-core microstructured optical fiber with a negative curvature of the core boundary in the spectral region >3.5 μm," Opt. Express **19**(2), 1441–1448 (2011)..
14. F. Yu, W. J. Wadsworth, and J. C. Knight, "Low loss silica hollow core fibers for 3–4 μm spectral region," Opt. Express **20**(10), 11153–11158 (2012)..
15. S. F. Gao, Y.-Y. Wang, W. Ding, D.-L. Jiang, S. Gu, X. Zhang, and P. Wang, "Hollow-core conjoined-tube negative-curvature fibre with ultralow loss," Nat. Commun. **9**(1), 2828 (2018)..
16. W. Belardi and J. C. Knight, "Hollow antiresonant fibers with reduced attenuation," Opt. Lett. **39**(7), 1853–1856 (2014)..
17. M. I. Hasan, N. Akhmediev, and W. Chang, "Positive and negative curvatures nested in an antiresonant hollow-core fiber," Opt. Lett. **42**(4), 703–706 (2017)..
18. A. N. Kolyadin, A. F. Kosolapov, A. D. Pryamikov, A. S. Biriukov, V. G. Plotnichenko, and E. M. Dianov, "Light transmission in negative curvature hollow core fiber in extremely high material loss region," Opt. Express **21**(8), 9514–9519 (2013)..
19. L. Vincetti and V. Setti, "Extra loss due to Fano resonances in inhibited coupling fibers based on a lattice of tubes," Opt. Express **20**(13), 14350–14361 (2012)..
20. B. Debord, A. Amsanpally, M. Chafer, A. Baz, M. Maurel, J. M. Blondy, E. Hugonnot, F. Scol, L. Vincetti, F. Gérôme, and F. Benabid, "Ultralow transmission loss in inhibited-coupling guiding hollow fibers," Optica **4**(2), 209–217 (2017)..
21. F. Poletti, "Nested antiresonant nodeless hollow core fiber," Opt. Express **22**(20), 23807–23828 (2014)..
22. M. S. Habib, J. E. Antonio-Lopez, C. Markos, A. Schülzgen, and R. Amezcua-Correa, "Single-mode, low loss hollow-core anti-resonant fiber designs," Opt. Express **27**(4), 3824–3836 (2019)..
23. H. Sakr, Y. Chen, G. T. Jasion, T. D. Bradley, J. R. Hayes, H. C. H. Mulvad, I. A. Davidson, E. Numkam Fokoua, and F. Poletti, "Hollow core optical fibres with comparable attenuation to silica fibres between 600 and 1100 nm," Nat. Commun. **11**(1), 6030 (2020)..
24. G. T. Jasion, T. D. Bradley, K. Harrington, H. Sakr, Y. Chen, E. Numkam Fokoua, I. A. Davidson, A. Taranta, J. R. Hayes, D. J. Richardson, and F. Poletti, "Hollow core NANF with 0.28 dB/km attenuation in the C and L bands," in *Optical Fiber Communication Conference Postdeadline Papers 2020*, (Optical Society of America, 2020), paper Th4B.4.
25. W. Belardi and J. C. Knight, "Hollow antiresonant fibers with low bending loss," Opt. Express **22**(8), 10091–10096 (2014)..
26. S.-F. Gao, Y.-Y. Wang, X.-L. Liu, W. Ding, and P. Wang, "Bending loss characterization in nodeless hollow-core anti-resonant fiber," Opt. Express **24**(13), 14801–14811 (2016)..
27. C. Wei, C. R. Menyuk, and J. Hu, "Bending-induced mode non-degeneracy and coupling in chalcogenide negative curvature fibers," Opt. Express **24**(11), 12228–12239 (2016)..
28. Y. Wang, M. I. Hasan, M. R. A. Hassan, and W. Chang, "Effect of the second ring of antiresonant tubes in negative-curvature fibers," Opt. Express **28**(2), 1168–1176 (2020)..
29. X. Huang, S. Yoo, and K. Yong, "Function of second cladding layer in hollow core tube lattice fibers," Sci. Rep. **7**(1), 1618 (2017)..
30. V. Setti, L. Vincetti, and A. Argyros, "Flexible tube lattice fibers for terahertz applications," Opt. Express **21**(3), 3388–3399 (2013)..
31. M. H. Frosz, P. Roth, M. C. Günendi, and P. S. J. Russell, "Analytical formulation for the bend loss in single-ring hollow-core photonic crystal fibers," Photonics Res. **5**(2), 88–91 (2017)..
32. R. M. Carter, F. Yu, W. J. Wadsworth, J. D. Shephard, T. Birks, J. C. Knight, and D. P. Hand, "Measurement of resonant bend loss in anti-resonant hollow core optical fiber," Opt. Express **25**(17), 20612–20621 (2017)..
33. A. F. Kosolapov, A. D. Pryamikov, A. S. Biriukov, V. S. Shiryaev, M. S. Astrapovich, G. E. Snopatin, V. G. Plotnichenko, M. F. Churbanov, and E. M. Dianov, "Demonstration of CO_2-laser power delivery through chalcogenide-glass fiber with negative-curvature hollow core," Opt. Express **19**(25), 25723–25728 (2011)..

Optics EXPRESS

34. T. D. Bradley, Y. Wang, M. Alharbi, B. Debord, C. Fourcade-Dutin, B. Beaudou, F. Gerome, and F. Benabid, "Optical properties of low loss (70 dB/km) hypocycloid-core kagome hollow core photonic crystal fiber for Rb and Cs based optical applications," J. Lightwave Technol. **31**(16), 2752–2755 (2013)..
35. B. Beaudou, A. Bhardwaj, T. D. Bradley, M. Alharbi, B. Debord, F. Gerôme, and F. Benabid, "Macro bending losses in single-cell kagome-lattice hollow-core photonic crystal fibers," J. Lightwave Technol. **32**(7), 1370–1373 (2014)..
36. J. Olszewski, M. Szpulak, and W. Urbanczyk, "Effect of coupling between fundamental and cladding modes on bending losses in photonic crystal fibers," Opt. Express **13**(16), 6015–6022 (2005)..
37. M. Heiblum and J. Harris, "Analysis of curved optical waveguides by conformal transformation," IEEE J. Quantum Electron. **11**(2), 75–83 (1975)..
38. R. T. Schermer and J. H. Cole, "Improved bend loss formula verified for optical fiber by simulation and experiment," IEEE J. Quantum Electron. **43**(10), 899–909 (2007)..
39. A. Deng, I. Hasan, Y. Wang, and W. Chang, "Analyzing mode index mismatch and field overlap for light guidance in negative-curvature fibers," Opt. Express **28**(19), 27974–27988 (2020)..
40. E. A. J. Marcatili and R. A. Schmeltzer, "Hollow metallic and dielectric waveguides for long distance optical transmission and lasers," Bell Syst. Tech. J. **43**(4), 1783–1809 (1964)..
41. A. Deng and W. Chang, "Geometrical scaling of antiresonant hollow-core fibers for mid-infrared beam delivery," Crystals **11**(4), 420 (2021)..
42. P. Uebel, M. C. Günendi, M. H. Frosz, G. Ahmed, N. N. Edavalath, J.-M. Ménard, and P. S. J. Russell, "Broadband robustly single-mode hollow-core PCF by resonant filtering of higher-order modes," Opt. Lett. **41**(9), 1961–1964 (2016)..